

**Characterization of the scission point from fission-fragment velocities**

M. Caamaño,<sup>1,2,\*</sup> F. Farget,<sup>1,2,†</sup> O. Delaune,<sup>1,‡</sup> K.-H. Schmidt,<sup>1</sup> C. Schmitt,<sup>1</sup> L. Audouin,<sup>3</sup> C.-O. Bacri,<sup>3</sup> J. Benlliure,<sup>2</sup> E. Casarejos,<sup>4</sup> X. Derkx,<sup>1,§</sup> B. Fernández-Domínguez,<sup>5</sup> L. Gaudefroy,<sup>6</sup> C. Golabek,<sup>1,||</sup> B. Jurado,<sup>7</sup> A. Lemasson,<sup>1</sup> D. Ramos,<sup>2</sup> C. Rodríguez-Tajes,<sup>2,1</sup> T. Roger,<sup>1</sup> and A. Shrivastava<sup>1,8</sup>

<sup>1</sup>GANIL, CEA/DSM-CNRS/IN2P3, BP 55027, F-14076 Caen Cedex 5, France

<sup>2</sup>Universidad de Santiago de Compostela, E-15706 Santiago de Compostela, Spain

<sup>3</sup>IPN Orsay, IN2P3/CNRS-UPS, F-91406 Orsay Cedex, France

<sup>4</sup>Universidad de Vigo, E-36310 Vigo, Spain

<sup>5</sup>University of Liverpool, Liverpool L69 7ZE, United Kingdom

<sup>6</sup>CEA DAM DIF, F-91297 Arpajon, France

<sup>7</sup>CENBG, IN2P3/CNRS-UBI, F-33175 Gradignan Cedex, France

<sup>8</sup>Nuclear Physics Division, Bhabha Atomic Research Centre, Mumbai 400085, India

(Received 6 May 2015; revised manuscript received 31 July 2015; published 14 September 2015)

The isotopic yield distributions and kinematic properties of fragments produced in the transfer-induced fission of  $^{240}\text{Pu}$  and fusion-induced fission of  $^{250}\text{Cf}$ , with 9 MeV and 45 MeV excitation energy, respectively, were measured in inverse kinematics with the spectrometer VAMOS. The kinematics of identified fission fragments allow to derive properties of the scission configuration such as the distance between fragments, the total kinetic energy, the neutron multiplicity, the total excitation energy, and, for the first time, the proton- and neutron-number sharing during the emergence of the fragments. These properties of the scission point are studied as functions of the fragment atomic number. The correlation between these observables, gathered in one single experiment and for two different fissioning systems at different excitation energies, give valuable information for the understanding and modeling of the fission process.

DOI: [10.1103/PhysRevC.92.034606](https://doi.org/10.1103/PhysRevC.92.034606)

PACS number(s): 24.75.+i, 25.70.Jj

**I. INTRODUCTION**

Nuclear fission is a complex process where a number of different properties of the nucleus influences the characteristics of the resulting splitting. In general, experimental observations are limited to a few observables, making it difficult to isolate the impact of specific nuclear properties on the whole process. As an illustration, the fission-fragment mass yields have been measured intensively during the last decades, being in fact the result of the proton and neutron sharing between the two fragments. Isotopic yields have been accessible only for the light fragments [1,2] whereas techniques of delayed  $\gamma$ -spectroscopy led to measures limited in range and in precision [3]. A few years back, the measure of the complete distribution of the fragment atomic number was feasible when based on techniques involving inverse kinematics [4], leading to new observations that were not expected from the study of mass distributions [5–7]. Recently, the use of inverse kinematics using transfer- and fusion-induced fission [8] has given access to the isotopic distributions of fragments issued from well-defined fissioning systems. In this scenario, the neutron excess (defined as the neutron-to-proton ratio) of each fragment over the whole distribution is a new observable that allows the investigation of the neutron and proton sharing

between fragments during their emergence, the effect of shell structure, and the way both fragments share the total excitation energy. In order to reproduce the data, fission models need to make assumptions on the scission configuration (deformation and nucleon sharing) and the partition of excitation energy between both fragments. However, scission-point properties are very difficult to derive experimentally because the fragment detection occurs after neutron evaporation, hiding the exact neutron numbers of the fragments. In general, the elongation at scission of the fissioning system is revealed by the measure of the total kinetic energy [7] while the deformation of fragments and the sharing of the excitation energy is derived from neutron multiplicities measured either directly [9,10] or indirectly from the velocity and energy of both fragments measured in coincidence [11].

In the present paper, the kinematic properties of the fission fragments are used to trace back information on the original split at scission. Due to the advantages of inverse kinematics, the average neutron excess of the fragments can be derived experimentally for the first time, in addition to the total kinetic energy and the neutron multiplicities. These results put forward unique information on the resulting equilibrium of neutron and proton sharing in the elongation process up to the scission point. The distance between the fragments and their total excitation energy at scission are also determined and discussed.

**II. FISSION VELOCITIES**

The characteristics of the fragment distributions from the fission of two different compound nuclei,  $^{240}\text{Pu}$  and  $^{250}\text{Cf}$ ,

\*manuel.fresco@usc.es

†fanny.farget@ganil.fr

‡Present address: CEA DAM DIF, F-91297 Arpajon, France.

§Present address: Universität Mainz, D-55128 Mainz, Germany.

||Present address: CEA, Centre de Saclay, IRFU/SPHN, F-91191 Gif-sur-Yvette, France.

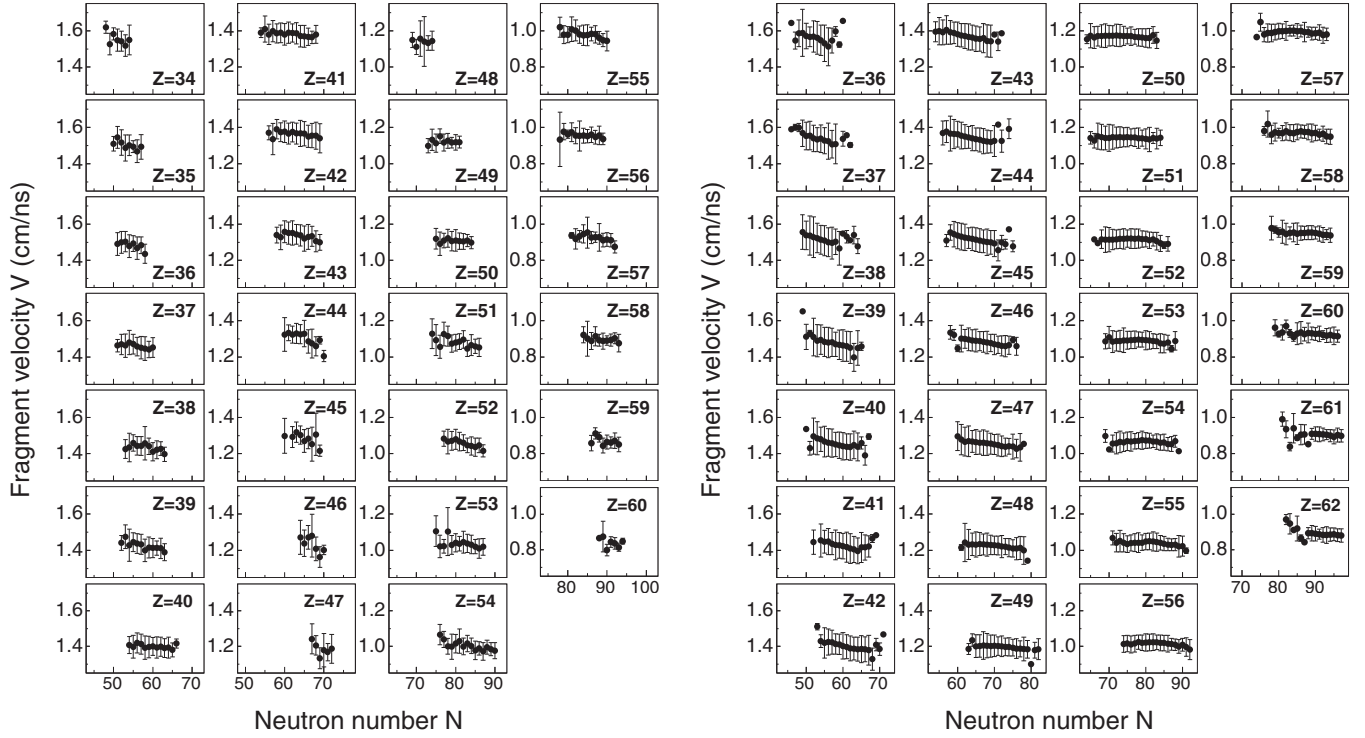


FIG. 1. Fission fragment velocity as a function of the neutron number of the elements produced in the fission of  $^{240}\text{Pu}$  (left panels) and  $^{250}\text{Cf}$  (right panels). The error bars show the second momentum of the velocity.

have been recently measured [8]. Both fissioning systems were produced using a  $^{238}\text{U}$  beam impinging onto a  $^{12}\text{C}$  target at 6.1A MeV, an energy 10% above the Coulomb barrier. The fusion channel produces the  $^{250}\text{Cf}$  system with an excitation energy of  $E^* \sim 45$  MeV. In the case of  $^{240}\text{Pu}$ , the fissioning system was populated in ( $^{12}\text{C}$ ,  $^{10}\text{Be}$ ) transfer reactions. The detection of the target-like nuclei allows the selection of the different reaction channels and, with the measurement of the energy and angle of the target-like nuclei, the excitation energy produced in the transfer reaction is reconstructed event by event [12]. In this work, it is assumed that all the excitation energy produced in the reaction is carried by the beam-like fissioning system. This approximation has been validated in a recent investigation of the transfer process between  $^{238}\text{U}$  and  $^{12}\text{C}$  [13]. Following this assumption,  $^{240}\text{Pu}$  was produced with an excitation energy distribution centered on  $E^* \sim 9$  MeV and a width of 6 MeV.

In the present paper, the calculation of the fission velocity is improved with respect to the previous work [8]: the slowing down of the fission fragments in the target is now taken into account following the prescription of Ref. [14], in which the different parameters are adjusted by means of LISE++ simulations [15]. In addition, the mean value of the velocity distribution of each fragment isotope has been corrected for transmission cuts (angle and ionic charge states) that can modify its calculation by few percents. The resulting fragment velocities in the reference frame of the fissioning nucleus  $V(A, Z)$  are displayed in Fig. 1 for the fission of  $^{240}\text{Pu}$  and  $^{250}\text{Cf}$ .

The average velocity  $\langle V \rangle$  as a function of the atomic number  $Z$  of the fragment is calculated with the isotopic yields  $Y(Z, A)$

as

$$\langle V \rangle(Z) = \frac{\sum_A V(Z, A) Y(Z, A)}{\sum_A Y(Z, A)}. \quad (1)$$

They are displayed in Fig. 2 for both systems. In addition to the experimental resolution and straggling, the error bars of  $\langle V \rangle(Z)$  include also the effect of the limits in the VAMOS acceptance: heavier fragments with low  $V(Z, A)$  are less transmitted, rendering mass distributions for each  $Z$  curtailed on their heavier part and thus cutting their associated velocities. These cuts tend to increase the value of the average velocity, modifying its value up to  $\sim 0.5\%$ . The magnitude of this effect

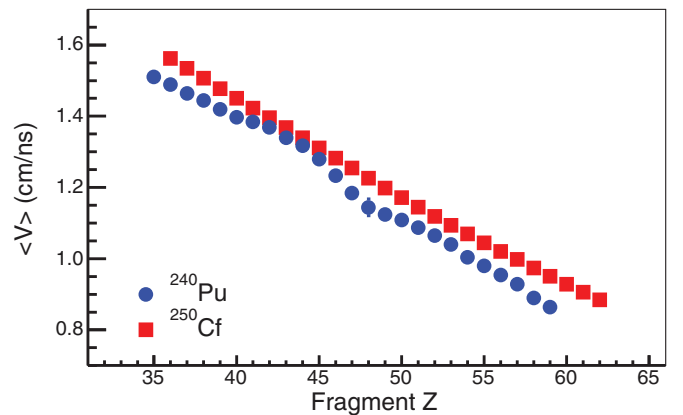


FIG. 2. (Color online) Average fragment velocity  $\langle V \rangle$  as a function of the fragment atomic number  $Z$  produced in the fission of  $^{240}\text{Pu}$  (blue dots) and  $^{250}\text{Cf}$  (red squares).

is estimated with the comparison of the measured distributions with those of a following experiment with the same reaction and an improved acceptance in VAMOS [16].

The steady decrease with increasing  $Z$ , observed for both cases, reveals the momentum conservation that induces smaller velocities as the mass of the fragment increases. In general, the velocities measured in the fission from  $^{250}\text{Cf}$  are between 2% and 10% larger than those of  $^{240}\text{Pu}$  due in part to the stronger Coulomb repulsion between the fragments. The oscillations in the fragment velocities from  $^{240}\text{Pu}$  are produced by structure effects that favor more compact configurations at scission for certain  $Z$ , increasing the velocities of the fragments with respect to the neighboring splits.

### III. RECONSTRUCTION OF THE FRAGMENT MASS AT SCISSION

The fission-fragment velocities contain information on properties of the scission configuration such as the elongation of the system and the masses of the nascent fragments. In the reference frame of the fissioning system and due to momentum conservation, the ratio of the two fragment velocities is equal to the inverse ratio of the initial masses  $M_{1,2}^*$  on each fission event:

$$\frac{V_1\gamma_1}{V_2\gamma_2} = \frac{M_2^*}{M_1^*} \quad (2)$$

with  $\gamma = [1 - (V/c)^2]^{-1/2}$ .

In the present experiment, the velocity of one single fragment per fission event is measured over the complete fragment production, therefore, it is not possible to derive the ratio of fragment velocity event by event. However, in both investigated cases, the excitation energy of the fissioning systems is not enough to allow proton evaporation along the fission process, therefore, for a fissioning system of atomic number  $Z_{\text{FS}}$ , the average characteristics of fragments with atomic number  $Z_1$  are correlated with the complementary atomic number  $Z_2 = Z_{\text{FS}} - Z_1$ . Under these conditions, the momentum conservation relates both fragments as

$$\langle V_1\gamma_1 M_1^* \rangle = \langle V_2\gamma_2 M_2^* \rangle, \quad (3)$$

where the observables with subscript 1 correspond to the fragments with atomic number  $Z_1$  and those with subscript 2 correspond to its complementary fragment  $Z_2$ .

The analysis of the measured fragments shows that  $\langle V_i\gamma_i M_i^* \rangle$  can be approximated to  $\langle V_i\gamma_i \rangle \langle M_i^* \rangle$  with a relative error smaller than 0.4%. The average values of mass excess permit to express  $\langle M_i^* \rangle$  as the product of the number of nucleons and the unified atomic mass unit,  $\langle M_i^* \rangle \approx u \langle A_i^* \rangle$ , with a deviation smaller than 0.1% in  $\langle A_i^* \rangle$ . In addition, a detailed simulation of the isotropic neutron evaporation by fragments, within ranges of velocity, mass, and  $Z$  as the ones measured, confirms that its effect on the fragment velocity is smaller than 0.15%. These approximations allow the use of the relation of Eq. (2) with the measured velocities averaged for each fragment:

$$\frac{\langle V_1\gamma_1 \rangle}{\langle V_2\gamma_2 \rangle} = \frac{\langle A_2^* \rangle}{\langle A_1^* \rangle}. \quad (4)$$

Assuming that no neutron evaporation occurs from saddle to scission nor from the neck at scission, and knowing the mass of the fissioning system  $A_{\text{FS}}$ , the average masses at scission can be deduced:

$$\langle A_1^* \rangle = A_{\text{FS}} \frac{\langle V_2\gamma_2 \rangle}{\langle V_1\gamma_1 \rangle + \langle V_2\gamma_2 \rangle}, \quad \langle A_2^* \rangle = A_{\text{FS}} - \langle A_1^* \rangle. \quad (5)$$

In the case of fission of  $^{240}\text{Pu}$  with  $E^* \sim 9$  MeV, no pre-scission neutron evaporation is considered; however, a contamination of 20% from  $^{241}\text{Pu}$  renders the final fissioning mass  $\langle A_{\text{FS}} \rangle = 240.2$ . In the case of  $^{250}\text{Cf}$ , the available excitation energy is sufficient to produce neutron evaporation before fission with a multiplicity that depends also on the angular momentum induced. Calculations based on the Bass model [17] were adjusted to reproduce the root-mean-square angular momentum induced in the  $^{16}\text{O} + ^{238}\text{U}$  reaction [18], where the angular momentum was derived from angular anisotropy of fission fragments. These calculations give an estimation of  $20\hbar$  in the case of the present fusion reaction. Considering this angular momentum and the initial  $E^* = 45$  MeV, the semi-empirical model GEF [19] gives an estimation of  $\langle A_{\text{FS}} \rangle = 249.6$ , with first-chance fission happening in more than 68% of the events. This result is consistent with the measurement of pre-scission neutrons emitted from a slightly lighter compound nuclei with similar excitation energy and larger angular momentum, for which a multiplicity of  $\sim 1$  is found [20]. The uncertainty estimated on  $\langle A_{\text{FS}} \rangle$  is limited to 0.3 mass units, considering possible small variations on the angular momentum and the validity of the model. The pre-scission neutron evaporation also modifies the average excitation energy of the fissioning system, estimated with the same code in  $E^* \sim 42$  MeV. It is important to note that the effect of any variation of the pre-scission neutron multiplicity on the quantities presented in this work (neutron excess, neutron multiplicity,  $TKE$ , etc.) concerns mostly to their overall magnitude, keeping their features unaffected.

The experimental neutron excess, that is the  $N$  over  $Z$  ratio, of the fission fragments is known to vary with the asymmetry of the fission split [2]: light fragments show a smaller neutron excess than the heavy fragments. This difference is known as the charge polarization. The neutron excess  $\langle N^* \rangle / Z$  at scission can be calculated with the average masses  $\langle A^* \rangle$  obtained in Eq. (5) as

$$\langle N^* \rangle / Z(Z) = \frac{\langle A^* \rangle (Z) - Z}{Z}, \quad (6)$$

and it is shown in Fig. 3 with full symbols for  $^{240}\text{Pu}$  and  $^{250}\text{Cf}$ . The deduced  $\langle N^* \rangle / Z$  at scission is compared in this figure with the measured  $\langle N \rangle / Z$  after neutron evaporation, shown in open symbols. In this case, the average  $\langle N \rangle$  is obtained from the measured masses and fragment yields as [8]

$$\langle N \rangle (Z) = \frac{\sum_A AY(Z, A)}{\sum_A Y(Z, A)} - Z. \quad (7)$$

The error bars in Fig. 3 of post-neutron evaporation  $\langle N \rangle / Z$  were also re-evaluated with respect to our previous analysis to account for cuts in the acceptance of the spectrometer. As in the case of the velocities, the effect of these cuts is evaluated with a following experiment with improved acceptance [16].

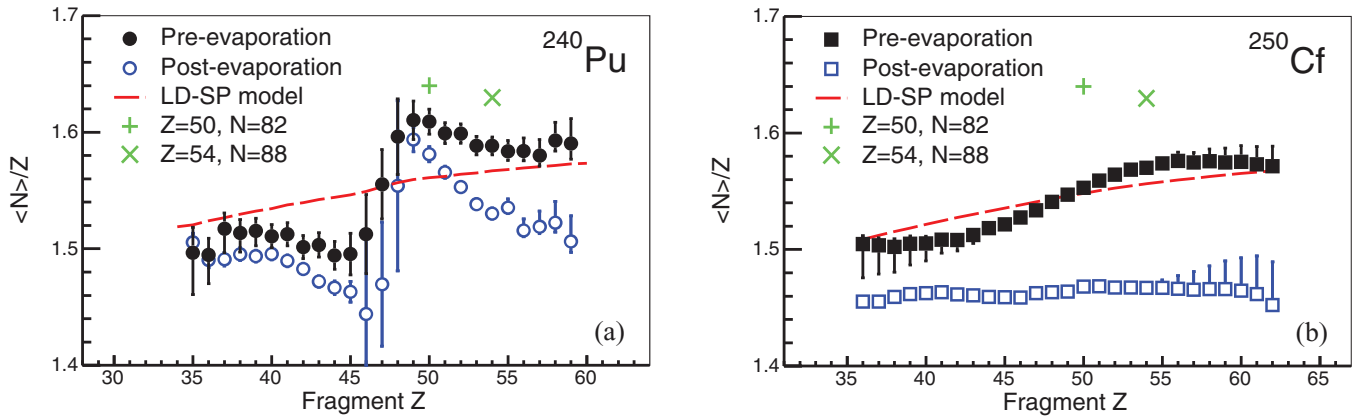


FIG. 3. (Color online) The average neutron excess  $\langle N \rangle / Z$  of fragments produced in the fission of  $^{240}\text{Pu}$  (a) and  $^{250}\text{Cf}$  (b) as a function of their atomic number  $Z$  is displayed before (black markers) and after (blue open markers) post-scission neutron evaporation. The pre-evaporation  $\langle N \rangle / Z$  is compared to the estimation of a LD-SP model (red-dashed line). Specific configurations  $Z = 50, N = 82$  and  $Z = 54, N = 88$  are marked with green crosses.

In addition to the estimated deviation due to acceptance cuts, the error bars of pre-neutron evaporation  $\langle N^* \rangle / Z$  include the statistical uncertainty, and the evaluated uncertainty of both  $\langle A_{\text{FS}} \rangle$  and the fission velocity in the reference frame of the fissioning system. In the case of  $^{240}\text{Pu}$ , the large error bars around symmetry are mainly produced by the effect of reduced statistics associated to low yields.

The resulting  $\langle N^* \rangle / Z$  for fission of  $^{240}\text{Pu}$  shows a step behavior with a sudden increase that peaks around  $Z \sim 50$ , associated with a minimum around  $Z \sim 44$ , and a rather constant value for higher  $Z$ .

The subsequent neutron evaporation does not modify the sudden increase in neutron excess at  $Z \sim 50$  (open symbols in Fig. 3), but a decrease is observed for  $Z > 50$ . In the case of fission of  $^{250}\text{Cf}$ , the neutron excess at scission shows a smooth behavior and a steady increase with  $Z$ , while neutron evaporation modifies significantly the trend. The fragments observed after neutron evaporation show a rather constant neutron excess, with no charge polarization.

As a basic reference, the deduced  $\langle N^* \rangle / Z$  can be compared with a simplified calculation based on the scission-point model introduced by Wilkins *et al.* [21]: the most probable combination of neutron excess of both fragments is defined as the one that minimizes the total energy of the system. In order to highlight features due to nuclear structure, only macroscopic energies of the deformed fragments are considered, following the liquid-drop energy prescription of Myers and Swiatecki [22], including Coulomb interaction between the two touching fragments and neglecting their nuclear interaction. The results of this liquid-drop scission-point (LD-SP) calculation are displayed in Fig. 3 as the dashed line. They show a steady increase of the neutron excess of scission fragments with their atomic number, reflecting the need to increase the number of neutrons for counterbalancing the increasing Coulomb repulsion inside the heavier fragments.

The data from  $^{240}\text{Pu}$  with  $E^* \sim 9$  MeV show clear deviations from the LD-SP calculation due to the influence of the nuclear structure on the sharing of neutrons and protons. Fragments around  $Z \sim 50$  and above are produced

with  $\langle N^* \rangle / Z$  in agreement with standards I and II shell effects, usually considered in low-energy fission [4,23]. Green crosses in Fig. 3(a) show the neutron excess associated with the spherical and deformed shells around  $Z \sim 50, N \sim 82$  and  $Z \sim 54, N \sim 88$  [23]. After neutron evaporation, the deformed shells lose their influence on  $\langle N^* \rangle / Z$  as the fragments recover their ground-state deformation. In the case of  $^{250}\text{Cf}$  with  $E^* \sim 42$  MeV, the experimental  $\langle N^* \rangle / Z$  slightly deviates from the smooth behavior of LD-SP. It shows a kind of “S” shape that renders the heavier fragments a little more neutron rich, and thus lighter fragments less neutron rich, than expected from equilibration of simple macroscopic strengths. In this shape, the influence of the standard I (closed shell) has clearly disappeared, while a possible influence of a deformed shell around  $Z \sim 54, N \sim 88$  may be still present: the heavier part of  $\langle N^* \rangle / Z$  seems to lean towards  $N \sim 88$  [green cross in Fig. 3(b)], suggesting a remaining competition between macroscopic, liquid-drop behavior and single-particle effects. Apart from these deviations, the deduced  $\langle N^* \rangle / Z$  and the calculation of the simplified LD-SP model coincide for very asymmetric splits in both systems.

#### IV. POST-SCISSION NEUTRON EVAPORATION

In low-energy fission, the neutron multiplicity, usually measured as a function of the fragment mass, displays a characteristic saw-tooth pattern for different systems [10,24,25]. This shape is understood as the result of the excitation energy, including deformation energy, released when the scission fragments separate and recover their ground-state deformation [10,21]. For higher-energy fission, part of the added excitation energy might be evaporated during the saddle-to-scission path and the rest is shared among the two fragments at scission. Most of this additional energy is released after scission with evaporated neutrons, thus making the neutron multiplicity a probe of the energy sharing between the two fragments, including their deformations.

The difference between the scission mass deduced from the velocity properties and the measured mass at the focal plane

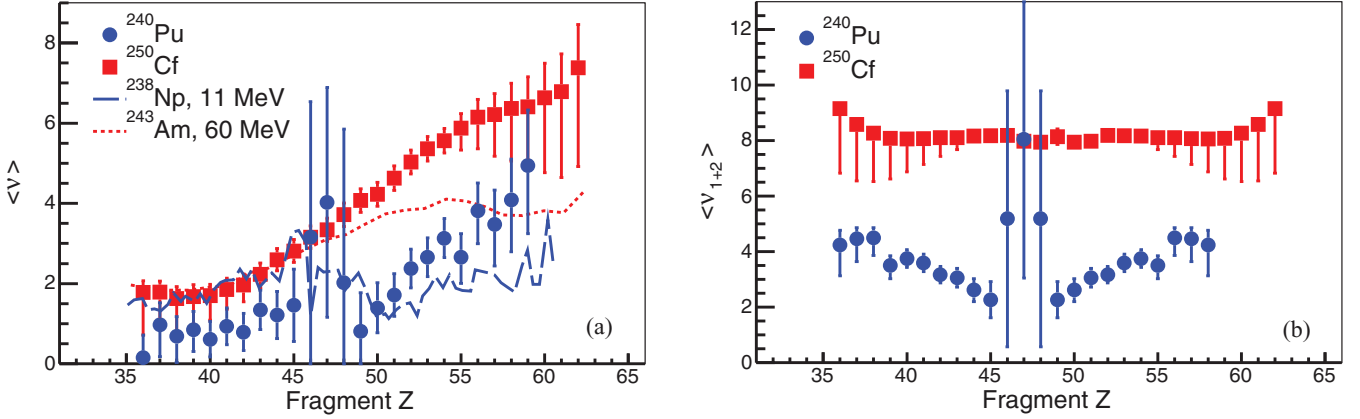


FIG. 4. (Color online) Average neutron multiplicity  $\langle \nu \rangle(Z)$  (a) and total neutron evaporation multiplicity  $\langle \nu_{1+2} \rangle(Z)$  (b) for  $^{240}\text{Pu}$  (blue dots) and  $^{250}\text{Cf}$  (red squares). Data from fission of  $^{238}\text{Np}$  with  $E^* \sim 11$  MeV (blue dashed line) [24] and  $^{243}\text{Am}$  with  $E^* \sim 6$  MeV (red dotted line) [26] are shown for reference.

of the spectrometer gives access to the average neutron multiplicity  $\langle \nu \rangle$  evaporated by the deformed scission fragments:

$$\langle \nu \rangle(Z) = \langle A^* \rangle(Z) - \langle A \rangle(Z). \quad (8)$$

The resulting average neutron multiplicities are shown in Fig. 4(a). Data from  $^{240}\text{Pu}$  are displayed with a previous measurement of  $^{238}\text{Np}$  at  $E^* \sim 11$  MeV. The saw-tooth behavior can be recognized in both systems, despite the large fluctuations that appear in the tails of the function and for symmetric splits of  $^{240}\text{Pu}$  (see Sec. III). The main feature of this behavior is a sudden minimum around  $Z \sim 50$ , where  $\langle N^* \rangle/Z$  displays a maximum. Considered together, both quantities suggest the formation of fragments around  $Z \sim 50$ ,  $N \sim 80$  that retain a small amount of excitation energy, indicating small deformations.

The experimental multiplicity  $\langle \nu \rangle$  of fission fragments of  $^{250}\text{Cf}$  at  $E^* \sim 42$  MeV, shown in Fig. 4(b), displays a steady increase with  $Z$ , in agreement with direct measurements in similar fusion-fission reactions [9,26]. The bend observed at  $Z \sim 54$  can also be seen in data from  $^{243}\text{Am}$  at  $E^* \sim 60$  MeV [26] (shown in the same figure) and it coincides with the top of the “S” shape observed in  $\langle N^* \rangle/Z$  (see Fig. 3). The large multiplicity indicates the formation of  $Z \sim 54$  fragments with large excitation energy.

The post-scission total neutron multiplicity per fission is defined as the sum of the multiplicities of fragment  $Z_1$  and its complementary  $Z_2 = Z_{\text{FS}} - Z_1$ , or the mass difference between the fissioning system and the fragments detected after neutron evaporation:

$$\langle \nu_{1+2} \rangle(Z) = \langle \nu_1 \rangle + \langle \nu_2 \rangle = A_{\text{FS}} - \langle A_1 \rangle - \langle A_2 \rangle. \quad (9)$$

The total multiplicity  $\langle \nu_{1+2} \rangle$  from fragments of  $^{240}\text{Pu}$  and  $^{250}\text{Cf}$  are shown in Fig. 4(b). In the case of  $^{240}\text{Pu}$ , it shows an average value around  $\langle \nu_{1+2} \rangle \approx 3$ , with a minimum around  $Z \sim 50$  and an increase for symmetric and very asymmetric splits, where the deformation of fragments is expected to be maximal. A very similar shape was already observed in thermal-neutron-induced fission of  $^{240}\text{Pu}$  [28]: a minimum found around mass  $A \sim 132$  was associated with the effect of the neutron shell  $N = 82$ . In the present case, the effect of

such neutron shell together with  $Z = 50$  proton shell seem to be present in the appearance of the minimum around  $Z \sim 50$ . In the case of  $^{250}\text{Cf}$ , a flat behavior without structure around  $\langle \nu_{1+2} \rangle \approx 8$  is observed. It is worth noting that some relevant features revealed in the study of  $\langle \nu \rangle$  are hidden in the case of the total multiplicity  $\langle \nu_{1+2} \rangle$ , particularly in the case of  $^{250}\text{Cf}$ .

## V. TOTAL KINETIC ENERGY AT SCISSION

The characteristics of the total kinetic energy distribution of fully accelerated fragments are mainly determined by the configuration of the system at scission (mass and charge split, deformations, and distance between the fragments). By using the fragment masses reconstructed at scission and their velocities, it is possible to derive the Coulomb potential energy that acts between the fragments that would be transformed in the total kinetic energy at scission ( $\langle TKE^* \rangle$ ) once the fragments are fully accelerated and before prompt-neutron emission. The average  $\langle TKE^* \rangle$  is calculated as

$$\langle TKE^* \rangle = u \langle A_1^* \rangle (\langle \gamma_1 \rangle - 1) + u \langle A_2^* \rangle (\langle \gamma_2 \rangle - 1). \quad (10)$$

The resulting  $\langle TKE^* \rangle$  as a function of  $Z$  is displayed in Fig. 5 for both fissioning systems. Ignoring the contribution of pre-scission velocity, the total kinetic energy at scission can be considered as the result of the Coulomb repulsion between the fragments at a distance  $D$ , which would depend on the deformations and the distance between the surface of the fragments [21]:

$$TKE^* = 1.44 \frac{Z_1 Z_2}{D}. \quad (11)$$

In Fig. 5(a), two clear peaks around  $Z \sim 50$  and  $Z \sim 44$  appear in the  $\langle TKE^* \rangle$  of  $^{240}\text{Pu}$ . These values of  $\langle TKE^* \rangle$ , higher by about 10 MeV with respect to symmetry, correspond to more compact shapes, and are usually interpreted as the result of the superposition of different fission modes corresponding to the formation of fragments with atomic closed shells [7]. The same features appear in thermal-neutron induced fission of  $^{239}\text{Pu}$  [27], also displayed in Fig. 5(a) as a dashed line.

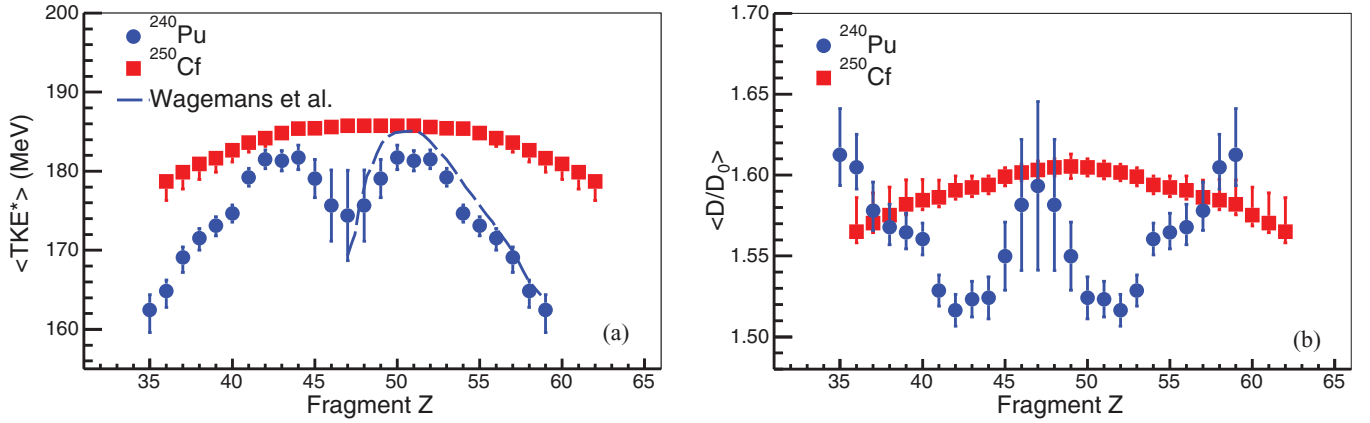


FIG. 5. (Color online) (a) Total kinetic energy of fission fragments at scission of  $^{240}\text{Pu}$  (blue dots) and  $^{250}\text{Cf}$  (red squares). The blue dashed line show data from thermal-neutron induced fission of  $^{239}\text{Pu}$  [27]. (b) Ratio of the distance between fragments at scission and that as spherical touching nuclei for fission of  $^{240}\text{Pu}$  (blue dots) and  $^{250}\text{Cf}$  (red squares).

In the case of  $^{250}\text{Cf}$ , structure effects are expected to vanish with its relatively high  $E^*$ , producing a smoother shape in  $\langle TKE^* \rangle$ . The measured  $\langle TKE^* \rangle$ , although smoother than that of  $^{240}\text{Pu}$ , shows an almost flat behavior around symmetric splits, between  $Z \sim 44$  and  $Z \sim 54$ , that hints at a reduced structure effect.

Following Eq. (11), the influence of structure in the  $\langle TKE^* \rangle$  is contained in the distance between the fragments. Its evolution can be seen and quantified more clearly considering the ratio of the actual distance  $D$  between the fragments at scission and their distance  $D_0$  as spherical touching nuclei. From Eq. (11), the average of this ratio  $\langle D/D_0 \rangle$  as a function of the fragment split can be calculated as

$$\langle D/D_0 \rangle = 1.44 \frac{Z_1 Z_2}{\langle TKE^* \rangle} \left( \frac{1}{r_0 \langle A_1^* \rangle^{1/3} + r_0 \langle A_2^* \rangle^{1/3}} \right) \quad (12)$$

with  $r_0 = 1.16$  fm. Figure 5(b) shows  $\langle D/D_0 \rangle$  for fission of both  $^{240}\text{Pu}$  and  $^{250}\text{Cf}$ . In the case of  $^{240}\text{Pu}$ , a clear anticorrelation appears between  $\langle TKE^* \rangle$  and  $\langle D/D_0 \rangle$ : the most compact shapes, with  $\langle D/D_0 \rangle \sim 1.5$ , appear around the maxima in  $\langle TKE^* \rangle$   $Z \sim 44$  and  $Z \sim 50$ , while at symmetric and very asymmetric splits, the elongation raises from values of 50% to 60% larger than the distance between the corresponding spherical touching fragments. The anticorrelation between  $\langle TKE^* \rangle$  and  $\langle D/D_0 \rangle$  observed in  $^{240}\text{Pu}$  disappears in the case of  $^{250}\text{Cf}$ . The elongation is kept around a value of  $\langle D/D_0 \rangle \sim 1.60$ , with a slight increase around symmetry and no apparent effects attributed to nuclear structure. The flat behavior of  $\langle TKE^* \rangle$  in  $^{250}\text{Cf}$  is not associated with any relevant feature in  $\langle D/D_0 \rangle$ .

## VI. TOTAL EXCITATION ENERGY AT SCISSION

The total energy available in the fission reaction  $E_{\text{tot}}$  is the sum of the mass of the fissioning system  $M_{\text{FS}}$  in its ground state and its excitation energy  $E_{\text{FS}}^*$ . At scission,  $E_{\text{tot}}$  is the sum of the masses of the fragments, the  $TKE^*$ , and the excitation of collective (deformation, rotation, etc.) and intrinsic (single-particle excitations) degrees of freedom. The experimental determination of  $\langle TKE^* \rangle$  at scission allows then

to determine the portion of the total energy that is transformed in the excitation energy of the fragments. Ignoring evaporation during the saddle to scission path, the conservation of  $E_{\text{tot}}$  links both instances:

$$E_{\text{tot}} = M_{\text{FS}} + E_{\text{FS}}^* = \langle M_1^* \rangle + \langle M_2^* \rangle + \langle TKE^* \rangle + \langle TXE^* \rangle, \quad (13)$$

where  $\langle M_i^* \rangle$  is the average ground-state mass of the fragment  $i$  and  $\langle TXE^* \rangle$  is the total excitation energy available for both fragments. The calculation of  $\langle M_i^* \rangle$  from the obtained  $\langle A_i^* \rangle$  is done by interpolation of the mass of the closest integer mass numbers:

$$\langle M_i^* \rangle = (1 - W_i) \cdot m_0(Z_i, \lfloor \langle A_i^* \rangle \rfloor) + W_i \cdot m_0(Z_i, \lfloor \langle A_i^* \rangle \rfloor + 1), \quad (14)$$

$$W_i = \langle A_i^* \rangle - \lfloor \langle A_i^* \rangle \rfloor,$$

where  $m_0(Z_i, A_i)$  is the ground-state mass of the isotope  $(Z_i, A_i)$  from the AME2012 evaluation [29]. The floor operator  $\lfloor \langle A_i^* \rangle \rfloor$  gives the largest integer not greater than  $\langle A_i^* \rangle$ .

The quantity  $\langle TXE^* \rangle$  can also be regarded as the difference between the total energy  $E_{\text{tot}}$  and the potential energy surface at scission. By subtracting  $E_{\text{FS}}^*$ , this difference can be expressed with respect to the ground state of the fissioning system as

$$\begin{aligned} \langle TXE_{\text{g.s.}}^* \rangle &= M_{\text{FS}} - \langle M_1^* \rangle - \langle M_2^* \rangle - \langle TKE^* \rangle \\ &= \langle Q_{\text{g.s.}} \rangle - \langle TKE^* \rangle, \end{aligned} \quad (15)$$

with  $\langle Q_{\text{g.s.}} \rangle$ , displayed in Figs. 6(a) and 6(b), as the difference between the average masses of the fissioning system and of the fragments at scission. The uncertainty on  $\langle Q_{\text{g.s.}} \rangle$  includes the estimated deviation of the calculation using  $\langle M_i^* \rangle$  from Eq. (14) compared with the calculation from actual mass distributions. This deviation is found to be below 2 MeV. Both systems exhibit a  $\langle Q_{\text{g.s.}} \rangle$  with a clear even-odd staggering, due to the systematic production of odd-odd or even-even  $Z$  pairs of fragments. The behavior of  $\langle Q_{\text{g.s.}} \rangle$  for each system is similar to that of their respective  $\langle TKE^* \rangle$  [see Figs. 6(a) and 6(b)], with two maxima around  $Z \sim 44$  and  $Z \sim 50$  in the case of  $^{240}\text{Pu}$  and a flatter top in the case of  $^{250}\text{Cf}$ . Figures 6(c) and 6(d) show the quantity  $\langle TXE_{\text{g.s.}}^* \rangle$  as a function of  $Z$  for  $^{240}\text{Pu}$

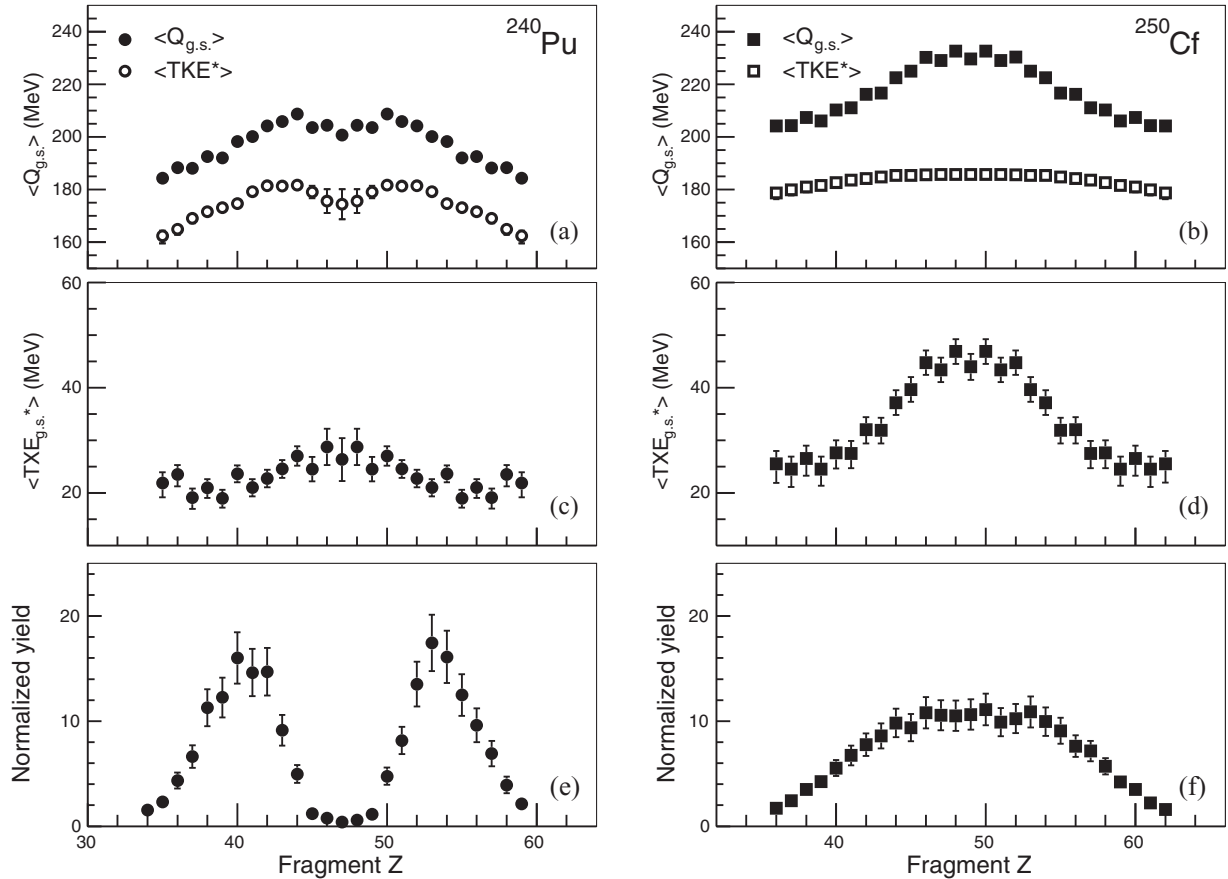


FIG. 6. (a), (b) Average difference between the ground states of the fissioning system and the fragments ( $\langle Q_{g.s.} \rangle$ ) at scission (full symbols) and the  $\langle TKE^* \rangle$  (open symbols). (c), (d) Total excitation energy at scission ( $\langle TXE_{g.s.}^* \rangle$ ). (e), (f) Post-neutron evaporation normalized yields for reference. (a), (c), and (e) correspond to  $^{240}\text{Pu}$  while (b), (d), and (f) correspond to  $^{250}\text{Cf}$ .

and  $^{250}\text{Cf}$ . Both fissioning systems show a similar behavior with a well-defined maximum centered at symmetric splits that raises from  $\sim 20$  up to  $\sim 25$  MeV in  $^{240}\text{Pu}$  and from  $\sim 25$  up to  $\sim 45$  MeV in  $^{250}\text{Cf}$ . In Ref. [30], a liquid-drop model (LDM) that considers surface, surface asymmetry, and Coulomb contributions is applied to thermal-neutron induced fission of  $^{239}\text{Pu}$ , resulting in a  $TXE_{g.s.}^* = 15.27$  MeV compared to  $\sim 25$  MeV determined in the present work. The same calculation applied to spontaneous fission of  $^{252}\text{Cf}$  results in  $TXE_{g.s.}^* = 24.94$  MeV, much smaller than the  $\sim 45$  MeV found for  $^{250}\text{Cf}$ .

The presented values of  $\langle D/D_0 \rangle$  and  $\langle TXE_{g.s.}^* \rangle$  as functions of  $Z$  [Figs. 5(b), 6(c), and 6(d)] can be interpreted as the shape of the energy potential that the fissioning system experiences at scission. In both systems, symmetric splits are characterized by elongated shapes and maxima in  $\langle TXE_{g.s.}^* \rangle$ . In the case of  $^{240}\text{Pu}$ , signatures of the most produced asymmetric yields, around  $Z \sim 42$  and  $Z \sim 52$ , are well correlated with shorter distances between the fragments and features in  $\langle TKE^* \rangle$  around  $Z \sim 44$  and  $Z \sim 50$  [see Fig. 5(a)], interpreted in previous sections as the effect of nuclear structure. However, the deduced  $\langle TXE_{g.s.}^* \rangle$  for the same system does not show any distinct behavior around these atomic numbers: the maxima in  $\langle TKE^* \rangle$  and  $\langle Q_{g.s.} \rangle$  compensate when both are subtracted

to calculate  $\langle TXE_{g.s.}^* \rangle$ , leaving a smooth evolution with the fragment split.

The total excitation energy gained at scission is released by the fragments via neutron and  $\gamma$  evaporation until their ground state is reached. The energy needed to evaporate these neutrons is the sum of their binding energies and their kinetic energy (a distribution between 0 and few MeV; see [9,10] for instance). Therefore, the sum of the separation energies of the evaporated neutrons  $E_v^{\min}$  is a lower limit for the energy released by neutron evaporation that can be calculated from the neutron multiplicity  $\langle \nu \rangle$  (see Sec. IV) and the post- and pre-evaporation masses as a function of the fragment  $Z$ :

$$E_v^{\min}(Z) = \langle M \rangle(Z) + m_n \cdot \langle \nu \rangle(Z) - \langle M^* \rangle(Z). \quad (16)$$

Figure 7 shows  $E_v^{\min}(Z)$  for both systems. Their behavior is similar to the ones observed in the neutron multiplicity in Fig. 4: in the case of  $^{240}\text{Pu}$ , the minimum energy released shows a saw-tooth behavior and a sudden minimum at  $Z \sim 50$ , while  $^{250}\text{Cf}$  shows a steady increase with the heaviest fragments releasing more excitation energy in the form of neutron evaporation. This increase is disturbed by a small decrease between  $Z \sim 52$  and  $56$ , produced by the difference between pre- and post-neutron evaporation masses of fragments with deformed ground states. For fission with high  $E_{\text{FS}}^*$ , where structure effects vanish, and considering the nascent fragments

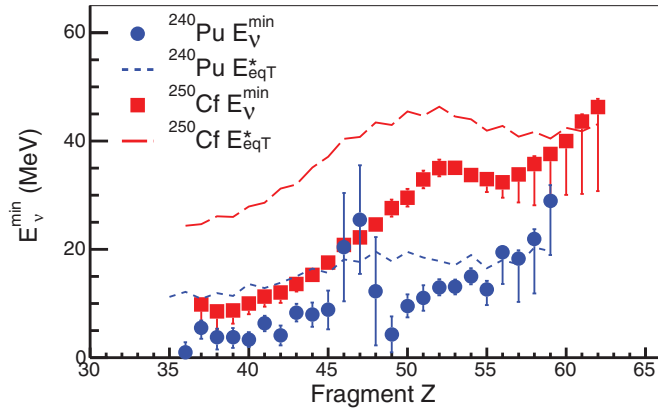


FIG. 7. (Color online) Minimum energy released in neutron evaporation and excitation energy shared according with the mass ratio of the fragments for  $^{240}\text{Pu}$  (blue dots and dashed line) and  $^{250}\text{Cf}$  (red squares and long-dashed line).

as two Fermi gas systems in statistical equilibrium, it is expected that the total  $TXE$  is shared between the fragments according with their mass ratio at scission [31]:

$$E_{\text{eqT}}^*(Z) = \langle TXE^* \rangle \frac{(A^*)(Z)}{A_{\text{FS}}}, \quad (17)$$

where  $E_{\text{eqT}}^*$  is the total excitation energy of fragment  $Z$  in this prescription. Figure 7 compares the deduced  $E_{\nu}^{\text{min}}$  with  $E_{\text{eqT}}^*$ . In both systems, the  $E_{\nu}^{\text{min}}$  of heavier fragments reaches similar values as their corresponding  $E_{\text{eqT}}^*$ , while light fragments take less than the half of it. This behavior suggests that, in both cases, the sharing of the excitation energy between both fragments is more asymmetric than suggested by Eq. (17). This observation is in agreement with a recent description of the energy partition in fission [32], based on the constant temperature level density [33], where it is shown that the statistical equilibrium between both fragments leads to a continuous flow of  $E^*$  from the light to the heavy fragments due to their unbalanced temperatures.

## VII. CONCLUSIONS

With the new generation of high-quality fission data obtained in inverse kinematics, new observables of the fission process are available. In addition to the fragment isotopic yields [8], the measurement of the fragment velocities in the fissioning-system reference frame allows to reconstruct the total kinetic energy  $\langle TKE^* \rangle$  and average masses of the two fragments at scission, both as a function of the fragment atomic number. In this work, the neutron excess of fragments is determined at scission for two different fissioning systems,  $^{240}\text{Pu}$  and  $^{250}\text{Cf}$ , with different excitation energies. For the first time, an experimental insight on the proton and neutron sharing during the elongation process is put forward. In addition, the

measurement of the total kinetic energy at scission allows the determination of the distance between fragments and the total excitation energy available.

In the low-energy fission of  $^{240}\text{Pu}$ , the neutron excess at scission displays a step behavior that favors the production of isotopes close to  $N \sim 82$  and  $N \sim 88$  for  $Z \sim 50$  and  $Z \sim 54$  fragments. At the same time, a minimum in the neutron multiplicity at scission and the most compact scission configuration appear at  $Z \sim 50$ . These three observations suggest the influence of  $N = 82$ ,  $Z = 50$  spherical shells in the formation of scission configurations with low excitation energy and smaller deformation than its neighbors. The relatively high excitation energy of  $^{250}\text{Cf}$ , with  $E^* \sim 45$  MeV, is expected to wash out the effect of shell structure at the scission point. The reconstructed neutron excess displays some features located around  $Z \sim 54$  not expected by simple macroscopic considerations, that could originate from a persistence of the effect of deformed shells. The neutron multiplicity shows a continuous increase as a function of  $Z$  while the distance between the fragments follows a smooth, almost constant, behavior. Together, these features indicate that the possible influence of deformed shells is associated to a scission configuration with high excitation energy and deformation of the same order as observed from the liquid-drop deformation.

The calculation of the  $\langle Q_{\text{g.s.}} \rangle$  for fission of  $^{240}\text{Pu}$  shows similar features to those found in  $\langle TKE^* \rangle$ . These structures compensate when subtracted to estimate the total excitation energy  $\langle TXE_{\text{g.s.}}^* \rangle$  released in fission. This leads to an almost constant energy release of about  $\langle TXE_{\text{g.s.}}^* \rangle \sim 25$  MeV over the complete fragment distribution. The symmetric fission is observed to be associated with a slightly more energetic release of almost 30 MeV. In the higher-energy fusion-induced fission of  $^{250}\text{Cf}$ , a strong evolution of  $\langle TXE_{\text{g.s.}}^* \rangle$  is observed, with 25 MeV more excitation energy in the symmetric splits than in the very asymmetric splits.

The calculation of a lower limit of excitation energy released by neutron evaporation as a function of  $Z$  suggests that the partition of  $TXE^*$  between the fragments according to their masses is not valid for these systems with  $E_{\text{FS}}^* \sim 9$  and  $\sim 42$  MeV; being more suitable the description with unbalanced temperatures and continuous flow of energy from the light to the heavy fragment [32].

## ACKNOWLEDGMENTS

M. Rejmund and A. Navin are acknowledged for their strong support during the experiment. M.C. was financially supported by the Programme “Ramón y Cajal” of the Spanish Ministerio de Economía y Competitividad. C.R.-T. was financially supported by the Programme “Axudas de apoio a etapa postdoutoral do plan galego de investigación, innovación e crecemento (Plan I2C)” of the Xunta de Galicia.

[1] W. Lang, H.-G. Clerc, H. Wohlfarth, H. Schrader, and K.-H. Schmidt, *Nucl. Phys. A* **345**, 34 (1980).

[2] J.-P. Bocquet and R. Brissot, *Nucl. Phys. A* **502**, 213 (1989), and references therein.

- [3] A. Bail *et al.*, *Phys. Rev. C* **84**, 034605 (2011).
- [4] K.-H. Schmidt *et al.*, *Nucl. Phys. A* **665**, 221 (2000).
- [5] S. Steinhäuser *et al.*, *Nucl. Phys. A* **634**, 89 (1998).
- [6] K.-H. Schmidt *et al.*, *Nucl. Phys. A* **685**, 60c (2001).
- [7] C. Böckstiegel *et al.*, *Nucl. Phys. A* **802**, 12 (2008).
- [8] M. Caamaño *et al.*, *Phys. Rev. C* **88**, 024605 (2013).
- [9] D. J. Hinde, D. Hilscher, H. Rossner, B. Gebauer, M. Lehmann, and M. Wilpert, *Phys. Rev. C* **45**, 1229 (1992).
- [10] K. Nishio, Y. Nakagome, H. Yamamoto, and I. Kimura, *Nucl. Phys. A* **632**, 540 (1998).
- [11] R. Müller, A. A. Naqvi, F. Käppeler, and F. Dickmann, *Phys. Rev. C* **29**, 885 (1984).
- [12] X. Derkx *et al.*, *EPJ Web Conf.* **2**, 07001 (2010).
- [13] C. Rodríguez-Tajes *et al.*, *Phys. Rev. C* **89**, 024614 (2014).
- [14] J. Dufour *et al.*, *Nucl. Instrum. Methods Phys. Res. A* **248**, 267 (1986).
- [15] D. Bazin, O. Tarasov, M. Lewitowicz, and O. Sorlin, *Nucl. Instrum. Methods Phys. Res. A* **482**, 307 (2002).
- [16] D. Ramos *et al.*, *Acta Phys. Pol. B* **46**, 443 (2015).
- [17] I. Gontchar, L. A. Litnevsky, and P. Fröbrich, *Comp. Phys. Comm.* **107**, 223 (1997).
- [18] B. B. Back *et al.*, *Phys. Rev. C* **32**, 195 (1985).
- [19] K.-H. Schmidt, B. Jurado, and Ch. Amouroux, General description of fission observables, GEF model, JEFF Report No. 24, NEA Data Bank of the OECD (2014); code version 2015-v1.2 4/2015.
- [20] A. Saxena, A. Chatterjee, R. K. Choudhury, S. S. Kapoor, and D. M. Nadkarni, *Phys. Rev. C* **49**, 932 (1994).
- [21] B. D. Wilkins, E. P. Steinberg, and R. R. Chasman, *Phys. Rev. C* **14**, 1832 (1976).
- [22] W. D. Myers and W. J. Swiatecki, *Ark. Fys.* **36**, 343 (1967).
- [23] U. Brosa, S. Grossmann, and A. Müller, *Phys. Rep.* **197**, 167 (1990).
- [24] A. A. Naqvi, F. Käppeler, F. Dickmann, and R. Müller, *Phys. Rev. C* **34**, 218 (1986).
- [25] C. Tsuchiya *et al.*, *J. Nucl. Sci. Tech.* **37**, 941 (2000).
- [26] E. M. Kozulin *et al.*, in *FUSION06: Reaction Mechanisms and Nuclear Structure at the Coulomb Barrier*, edited by L. Corradi, D. Ackermann, E. Fioretto, A. Gadea, F. Haas, G. Pollarolo, F. Scarlassara, S. Szilner, and M. Trotta, AIP Conf. Proc. No. 853 (AIP, New York, 2006), p. 336.
- [27] C. Wagemans, E. Allaert, A. Deruytter, R. Barthélémy, and P. Schillebeeckx, *Phys. Rev. C* **30**, 218 (1984).
- [28] V. F. Apalin, Yu. N. Gritsyuk, I. E. Kutikov, V. I. Lebedev, and L. A. Mikaelian, *Nucl. Phys.* **71**, 553 (1965).
- [29] G. Audi *et al.*, *Chinese Phys. C* **36**, 1287 (2012).
- [30] M. Asghar and R. W. Hasse, *J. Phys. (Paris)* **45**, C6-455 (1984).
- [31] J. Toke and W. U. Schröder, *Annu. Rev. Nucl. Sci.* **42**, 401 (1992).
- [32] K.-H. Schmidt and B. Jurado, *Phys. Rev. Lett.* **104**, 212501 (2010).
- [33] A. Gilbert and A. G. W. Cameron, *Can. J. Phys.* **43**, 1446 (1965); P. J. Brancazio and A. G. W. Cameron, *ibid.* **47**, 1029 (1969).